Probing gas-surface potential energy surfaces with diffraction of hydrogen molecules

2002 J. Phys.: Condens. Matter 14 6037

(http://iopscience.iop.org/0953-8984/14/24/309)

INSTITUTE OF PHYSICS PUBLISHING JOURNAL OF PHYSICS: CONDENSED MATTER

J. Phys.: Condens. Matter **14** (2002) 6037–6064 PII: S0953-8984(02)36286-6

Probing gas–surface potential energy surfaces with diffraction of hydrogen molecules

M F Bertino[1,2] **and D Farías**[3]

[1] Department of Physics, University of Missouri-Rolla, Rolla, MO 65401, USA
[2] Max-Planck-Institut für Strömungsforschung, Bunsenstrasse 10, 37073 Göttingen, Germany
[3] Departamento de Física de la Materia Condensada, C-III and Instituto Nicolás Cabrera, Universidad Autónoma de Madrid, Cantoblanco, 28049 Madrid, Spain

E-mail: massimo@umr.edu and daniel.farias@uam.es

Received 26 April 2002
Published 31 May 2002
Online at stacks.iop.org/JPhysCM/14/6037

Abstract

We review recent experiments where diffraction of deuterium molecules from single-crystal surfaces was employed to characterize the potential energy surface for hydrogen dissociative chemisorption. Scattering experiments were carried out on Cu(001), which is the prototype of a system with a high barrier for dissociative chemisorption, on Ni(110), which is the prototype of a system with a low barrier, and on NiAl(110), which is the prototype of an alloy surface with a high barrier. The experiments were carried out on two different set-ups at incident energies between about 20 and 250 meV. Elastic and rotationally inelastic diffraction (RID) peaks were observed in all experiments. Diffraction probabilities are presented and compared for each surface. Elastic diffraction intensities were interpreted with a simple corrugated hard-wall scattering potential. The values of the corrugation are $h = 0.075$ Å for D_2/Cu(001), and $h = 0.091$ Å for D_2/Ni(110). A satisfactory fit of the diffraction intensities could be obtained for D_2/NiAl(110) only over a very limited range of incident beam energies. A major finding of our experiments is that dissociative chemisorption strongly affects RID probabilities. These are higher by about a factor of 3–5 for scattering from Ni(110) than for the high-barrier systems Cu(001) and NiAl(110). The high rotational transition probability for systems with low barrier is interpreted as a consequence of the angular anisotropy of the chemisorption potential. Perspectives for future experiments are discussed.

Contents

1. Introduction

Scattering of thermal energy projectiles from surfaces provides a powerful method of surface characterization, which has the best-known variation in He-atom scattering [1, 2]. Compared to He scattering, hydrogen scattering does not allow high-resolution time-of-flight (TOF) measurements, and is not well suited to investigate dynamic processes at surfaces, such as vibrations and adsorbate diffusion. For this reason, hydrogen scattering was mostly employed in early studies, and then only to determine more 'static' properties. These include measurements of the geometric corrugation with diffraction experiments, and measurements of the hydrogen–surface interaction potential via scattering resonances. These studies have established that, in general, the corrugation amplitudes and interaction potentials are larger for H_2 than for He. These differences are a consequence of the larger polarizability of H_2 molecules, which gives rise to a stronger attractive interaction [3]. Values of the geometric corrugation amplitude h and potential well depth ϵ are listed in table 1 for several transition metal surfaces. One exception to the general trends is the Ag(110) surface, where a larger corrugation was observed with He than with H_2 [4]; the origin of this behaviour is not clear at present. A similar effect was observed for MgO(001) by Kolodney and Amirav [5], who reported corrugation amplitudes of 0.16 and 0.11 Å along the [100] azimuth for He and H_2, respectively.

Also, weak diffraction peaks, originating from rotationally inelastic transitions, can be detected when diatomic molecules are scattered from surfaces. In these rotationally inelastic diffraction (RID) peaks, the incident molecules convert part of their translational energy into excitation of a rotational quantum level when colliding with the surface. This phenomenon leads to additional diffraction peaks in the angular distributions. The position of these RID peaks within an angular distribution can be obtained by combining the Bragg condition for surface diffraction with conservation of energy [4]:

$$\begin{aligned} \Delta\vec{K} &= \vec{K}_f - \vec{K}_i = \vec{G} \\ E_f - E_i &= \Delta E_{rot}. \end{aligned} \tag{1.1}$$

In (1.1), $\vec{K}_f$ and $\vec{K}_i$ are the parallel components of the outgoing and incident wavevectors, respectively, $\vec{G}$ is a surface reciprocal-lattice vector, E_f and E_i the final and incident beam energies, and ΔE_{rot} is the rotational transition energy. For H_2 (D_2) this energy is $|\Delta E_{rot}| = 44.6$ (22.2) meV for the lowest transitions ($0 \to 2$ and $2 \to 0$) and $|\Delta E_{rot}| = 74.3$ (36.88) meV for the $1 \to 3$ and $3 \to 1$ transitions.

RID has been investigated in the past both theoretically and experimentally on the surfaces of ionic solids [6–10]. Only a few studies have been reported for H_2 and its isotopes on the

Table 1. Comparison of corrugation amplitudes h and well depths ϵ corresponding to the interaction potentials of He and H_2/D_2 beams with different clean, unreconstructed metal surfaces at the indicated energies. The values of the corrugation amplitude refer to the more corrugated surface directions. The values of ϵ have been derived from selective adsorption measurements, except for D_2/Ni(110) and D_2/NiAl(110), where they were obtained from a Debye–Waller fit to the data. For Rh(110), ϵ was not determined.

	He			H_2/D_2			
Surface	h (Å)	E_i (meV)	ϵ (meV)	h (Å)	E_i (meV)	ϵ (meV)	Reference
Cu(001)	$\leqslant 0.005$	15–250	5	0.061	77	31	[14]
				0.075	20–250		[15–18]
Cu(110)	0.13	77	6.3	0.216	77	31	[14, 19]
Ag(111)	0.022	65	5	0.06	55	32	[4, 20]
Ag(110)	0.27	65	6	0.11	75–135	31.7	[4, 21, 22]
Ni(111)	0.022	65	9	0.16	65	25	[23]
Ni(110)	0.060	20–90	5	0.091	25–90	45	[24, 25]
Rh(110)	0.15	65	8.5	0.166	71.5	—	[26, 27]
NiAl(110)	0.035	65	7	0.12	75–157	35	[28, 29]

low-index metal surfaces. For example, RID peaks have been clearly resolved for the strongly anisotropic HD molecules scattered from Pt(111) [11] and Ni(001) [12], and, more recently, from Cu(001) [13]. For the nearly spherical H_2 and D_2 molecules, RID manifests itself usually as weak shoulders in the flanks of the elastic diffraction peaks for H_2/Ag(111) [20], H_2/Ag(110) [4], and D_2/Cu(001) [30]. To our knowledge, only in the case of H_2 scattering from Ag(111) [31] were RID peaks previously clearly resolved.

Concerning the methods used to calculate RID probabilities, approximate calculations with different levels of accuracy have been reported. These approaches (usually tested with the H_2/LiF(001) system) include the eikonal approximation [6], the sudden approximation [7, 32–35], a semiclassical perturbation approach [36], a distorted-wave treatment for subsets of the internal states [37], and a non-perturbative method based on Gaussian wavepackets [38]. Like in the case of atom scattering, a disadvantage of these approximations is that their range of validity is in general not known, making a comparison with exact close-coupling calculation necessary. Such calculations were performed by Drolshagen *et al* [39] for H_2 scattering from LiF(001) and collision energies up to 0.7 eV, a much broader range than the one covered in the early (also exact) calculations reported by Wolken [40, 41]. A finite-temperature theory for calculating RID probabilities as a function of surface temperature was reported by Cruz and Jackson [42].

In recent years, inclusion of dissociative chemisorption has renewed interest in diffraction of hydrogen from surfaces. These calculations have shown that information on the dissociative chemisorption potential can not only be obtained by measuring the fraction of molecules that stick to the surface [43–45], but also, and perhaps more precisely, by analysing diffraction of molecules. The theoretical models used for describing the dynamics of molecular dissociation at surfaces have been reviewed by several authors and will not be considered here [46–50]. The theoretical results are often very intriguing, but are difficult to verify experimentally. Hydrogen diffraction from transition metal surfaces like Pt, Ni, or Pd can be measured, but, since dissociation is non-activated, a hydrogen overlayer builds up quickly and alters the measurements. To prevent formation of a hydrogen overlayer, experiments must be carried out at high surface temperatures, which increase the inelastic background and compel one to

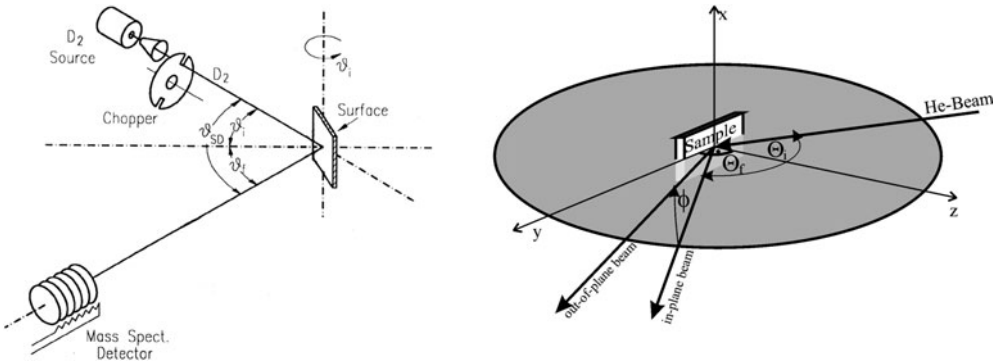

Figure 1. 'Fixed-angle' experimental set-up used in Göttingen (left). In the Berlin set-up (right) the detector can be rotated in and out of the scattering plane while keeping the angle of incidence fixed. In the Göttingen set-up, the angle of incidence is changed during a measurement by rotating the sample.

work at low beam energies. Diffraction from noble metals can be measured also, but hydrogen dissociation on these surfaces is activated, and high beam energies are required to overcome the barrier. Generation of highly energetic molecular beams with high velocity resolution is challenging, and very low surface temperatures are required to minimize inelastic background effects induced by the high incident energy.

It was not until very recently that hydrogen diffraction experiments were performed over a wide range of incident energies and with a resolution high enough to allow also investigation of RID peaks. Experiments were carried out on Ni(110) [24] and Cu(001) [15], which can be considered as models of systems with a low and a high barrier, respectively, and on NiAl(110) [29], which is a model system for an alloy surface. The main goal of this article is to summarize these results and to consider future experiments.

2. Experimental set-ups

The experiments were carried out on two separate set-ups. In one set-up, at the Max-Planck-Institut für Strömungsforschung, Göttingen, measurements were carried out with high angular resolution on single-crystal surfaces of Cu(001) and Ni(110). In the second set-up, at the Freie Universität Berlin, measurements were carried out with lower angular resolution, but fixed angle of incidence, on NiAl(110).

A schematic representation of the two set-ups is shown in figure 1. The Göttingen set-up shown on the left belongs to the class of 'fixed-angle' systems, where the angle between incident and outgoing beams is fixed, while the Berlin set-up allows rotation of the detector about two axes independent of the incident angle. Set-ups with a rotatable detector can measure diffraction peaks for a fixed angle of incidence, and make comparison with calculations easier. Another advantage of this class of set-ups is that they allow direct measurement of the incident beam intensity, making possible very accurate determination of absolute diffraction probabilities. On the other hand, since the detector lies very close to the sample, the angular resolution is lower than for 'fixed-angle' systems. Another disadvantage of this configuration is that it hardly allows for differential pumping of the detector, resulting in general in a smaller dynamical range of measured intensities as compared to the differentially pumped 'fixed-angle' systems used in TOF experiments.

2.1. Göttingen set-up

Scattering experiments were carried out with a high-resolution He-atom TOF spectrometer developed for measuring surface phonon dispersion curves [51,52]. The beam of D_2 molecules from a high-pressure free jet expansion passed through three differentially pumped chambers before impinging on the metal target in the UHV chamber. After scattering through a fixed angle of $\theta_{SD} = 95.76^\circ$ with respect to the incident beam, the particles were detected by a home-made magnetic mass spectrometer detector. Angular distributions were measured by rotating the crystal about an axis normal to the plane of the incident and outgoing beams. For this geometry the parallel momentum transfer $\Delta\vec{K}$ for elastic scattering is given by

$$\Delta\vec{K} = \vec{k}_i(\sin\theta_f - \sin\theta_i), \tag{2.1}$$

where $\vec{k}_i$ is the incident wavevector, θ_i is the incident angle measured with respect to the surface normal, and the final angle is given by $\theta_f = \theta_{SD} - \theta_i$. The overall angular resolution was 0.35° [51].

Scattering experiments were carried out at energies between about 20 and 250 meV. To cover this wide range of incident energies, two different nozzle beam sources were used. One source, designated the 'conventional source', was a high-pressure supersonic nozzle source with a $d = 10$ μm diameter orifice used in high-resolution He inelastic TOF measurements at low incident energies [51]. With this source the beam energy could be continuously varied between 10 and 110 meV by changing the source temperature T_0 in the range from 70 to 430 K. With D_2 beams the formation of clusters in the expansion limited the source pressure to $P_0 \leqslant 10$ bar ($P_0 d = 7.6$ Torr cm^{-1}) at $T_0 = 70$ K and to $P_0 \leqslant 100$ bar ($P_0 d = 76$ Torr cm^{-1}) at $T_0 = 180$ K [53]. For the conventional nozzle, P_0 was optimized to minimize the velocity spread of the incident beam which was measured typically to be about 1% for He and between 3% ($T_0 = 120$ K) and 8% ($T_0 = 70$ K) for D_2.

For the higher incident beam energies, $120 \leqslant E_i \leqslant 250$ meV, a second supersonic nozzle beam source, the 'hot source', was employed. This source consisted of a sapphire tube with an orifice of diameter $d = 74$ μm. The tube was heated by electron bombardment up to temperatures $T_0 \sim 1300$ K. A four-layer tantalum radiation shield was mounted around the sapphire tube to reduce power dissipation to about 50 W at the higher source temperatures. The radiation shield was kept at a negative potential with respect to the emitting filament to prevent electrons from reaching the D_2 beam. The skimmer was water cooled to prevent misalignments between the nozzle and skimmer axes due to radiative heating. The maximum source pressure was limited by the speed of the nozzle chamber diffusion pump to $P_0 = 15$ bar. The velocity resolution of the D_2 beam with the hot source was similar for He and D_2 and varied between 7% at $E_i = 130$ meV ($T_0 = 450$ K, $P_0 = 4$ bar) and 12% at $E_i = 250$ meV ($T_0 = 1100$ K, $P_0 = 14$ bar).

The Cu(001) and Ni(110) single-crystal surfaces employed in the Göttingen set-up were cleaned *in situ* with repeated cycles of ion sputtering and annealing [15, 24, 51]. Scattering experiments on Cu(001) were carried out at energies between 20 and 250 meV. To reduce the multiphonon background, the surface was maintained at a temperature $T_s = 60$ K for the measurements with D_2 ($T_s = 100$ K with He). After each measurement the crystal was heated to a temperature $T_s = 600$ K to desorb any adsorbed contaminant molecules. At incident beam energies E_i above 250 meV the diffracted intensity was observed to decrease over a period of about 10 min. This was attributed to dissociative chemisorption of D_2, and the measurements were limited to a maximum incident energy $E_i = 250$ meV.

On Ni(110), hydrogen dissociative chemisorption has probability close to unity. Due to the extreme sensitivity of diffraction intensities to the presence of adsorbates, the stationary surface coverage of hydrogen had to be minimized. The surface had to be maintained at

a temperature of 700 K to prevent the build-up of an adsorbed layer of D_2. To calculate the stationary coverage of D_2, one may proceed as follows. For a incident flux F_0, sticking coefficient s, and desorption constant k, the time derivative of the D_2 coverage θ is given by [54, 55]

$$\frac{d\theta}{dt} = 2sF_0 - 2k\theta^2. \tag{2.2}$$

For stationary conditions ($d\theta/dt = 0$), the coverage is simply: $\theta = \sqrt{sF_0/k}$. To obtain a conservative estimate, we assume $s = 1$ independent of coverage and surface temperature, and $F_0 = 10^{15}$ molecules cm^{-2} s^{-1} [51, 54]. The recombination constant k was experimentally measured for Ni(110) in [54] with the same apparatus as was employed for the diffraction measurements described here. For $T_s = 700$ K, $k \approx 1.43 \times 10^4$ and $\theta = 0.83\%$; while for $T_s = 600$ K, $k \approx 8.3 \times 10^3$ and $\theta = 1.1\%$. This estimate shows that, to avoid significant decrease of the scattered intensity due to adsorbed hydrogen, $T_s = 700$ K is the lowest temperature at which we felt it to be safe to take measurements. This high temperature increased the multiphonon background, and limited to about 100 meV the maximum incident energy for which diffraction peaks could be measured.

2.2. Berlin set-up

The atomic and molecular beam diffraction apparatus used in the laboratory in Berlin, and recently transferred to the surface science laboratory at the Universidad Autónoma de Madrid, is described in detail in [56]. Atomic and molecular beams are generated by supersonic expansion through a 1 mm diameter platinum tube in which a hole of approximately 8×10^{-2} mm diameter was spark eroded in the side. The tube is clamped between massive copper supports, and can be resistively heated to 1000 K and cooled to 100 K by contact with a liquid nitrogen reservoir. After expansion, the beam is collimated by a 0.5 mm diameter skimmer and traverses two differential pumping stages before entering the sample chamber. The beam was mechanically chopped with a magnetically coupled rotary motion feedthrough in the third stage to allow phase-sensitive detection.

The base pressure in the chamber is typically $\sim 3 \times 10^{-11}$ mbar, reaching $\sim 5 \times 10^{-10}$ mbar with the He or D_2 beam on. This pressure increase gives rise to a continuous background in the scattering chamber which limits the signal-to-noise ratio; the signal is recovered from the background by means of a lock-in system ($f \sim 100$ Hz). The sample is mounted on a manipulator that allows azimuthal rotation of the sample as well as heating to 1200 K and cooling to 100 K. The angular distribution of the scattered atoms was analysed with a quadrupole mass spectrometer mounted on a two-axis goniometer. A 1 mm aperture is placed in front of the quadrupole's filament, which is positioned at 5 cm from the sample. This arrangement allows rotations of 200° in the scattering plane, defined by the beam direction and the normal to the surface, and ±15° normal to the scattering plane. The ability to measure out-of-plane spectra is a valuable asset in interpreting diffraction data. Angles of incidence θ_i and angles of scattered beams θ_f are both referenced to the surface normal, whereas the out-of-plane angle ϕ is usually measured from the scattering plane.

The NiAl(110) sample was prepared in UHV with several cycles of sputtering and annealing [28, 57]. All data presented here refer to a scattering geometry in which the incident beam impinges perpendicular to the [001] symmetry direction of the substrate. We recall at this point that NiAl forms a compositionally ordered alloy in a CsCl structure, with an electronic structure consisting of a filled d band [58]. As a consequence, molecular hydrogen has an activation barrier for spontaneous dissociation of 0.72 eV [59]. The NiAl(110) surface is terminated by 50% Ni and 50% Al (see figure 2), and exhibits a rippled relaxation in which

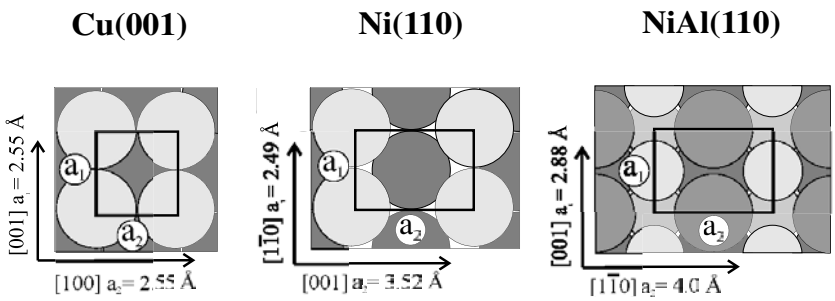

Figure 2. Top views of the surface unit cells of NiAl(110), Cu(001), and Ni(110) indicating the main symmetry directions.

the Ni atoms are contracted toward the bulk by roughly 6% of the bulk layer spacing (2 Å) while the Al atoms are expanded into the vacuum by 5% [60]. Figure 2 shows the structure, the main symmetry directions, and the first Brillouin zone of the clean NiAl(110) surface.

3. Procedure used to determine diffraction probabilities

We will illustrate in this section the procedure that we adopted to determine elastic and inelastic diffraction probabilities. Note that our nomenclature will slightly differ from that of previous publications [15,24]. In previous publications, we defined 'diffraction reflectivities' to indicate what, more conventionally, are defined as diffraction probabilities. Our definition derived from the method that we employed to determine incident beam intensities, which was based on the specularly reflected beam. In this paper, we will use the more conventional terminology and refer to diffraction probabilities.

3.1. Occupation of rotational levels in the incident beam

The presence of rotationally inelastic transitions makes determination of diffraction probabilities for molecules more complicated than for atoms. One main complication is the necessity to determine the occupation probability of the rotational levels in the incident beam.

A number of previous investigations [53,61–64] have shown that the rotational populations of the lowest rotational states of highly expanded supersonic molecular beams follow a nearly Boltzmann distribution which can be characterized by an effective rotational temperature T_R that is somewhat smaller than the source temperature T_0. The relation between T_R and T_0 is complex and depends not only on the parameter P_0d, where d is the nozzle orifice diameter, but also on T_0. To determine rotational temperatures in the incident beam over the very wide range of nozzle temperatures of our experiments, we followed the procedure described in [64]. Rotational populations of supersonic molecular beams can be interpolated by a logarithmically linearized correlation function, which, for H_2 expansion at $T_0 = 293$ K, is given by

$$\log(T_R/T_0) = -0.21\log(P_0d) + 0.043, \tag{3.1}$$

and, for D_2, by

$$\log(T_R/T_0) = -0.40\log(P_0d) + 0.16, \tag{3.2}$$

when P_0d is expressed in units of Torr cm. Equations (3.1) and (3.2) scale with the inverse Knudsen number $(Kn)^{-1} = P_0d/T_0$ for nozzle temperatures different from room

Table 2. Relative populations (in %) of the rotational levels j for D_2 nozzle beams for source conditions P_0d and source temperatures T_0 employed in the Ni(110) scattering experiment.

P_0d (Torr cm)	T_0 (K)	T_R (K)	$j=0$	$j=1$	$j=2$	$j=3$	$j=4$
76	180	56	63.0	33.0	4.0	0	0
76	300	77	57.0	32.7	9.3	0.25	0.01
76	400	115	43.2	31.1	23.4	1.9	0.3

Table 3. Relative populations (in %) of the rotational levels j for D_2 nozzle beams for source conditions P_0d and source temperatures T_0 employed in the NiAl(110) scattering experiment.

P_0d (Torr cm)	T_0 (K)	T_R (K)	$j=0$	$j=1$	$j=2$	$j=3$	$j=4$
24	300	136.3	38.0	30.0	28.4	2.9	0.6
24	400	203.9	26.4	25.6	37	7.1	3.4
24	500	278.6	19.8	21.4	39.1	10.6	8
24	600	359.7	15.8	18	38.4	12.7	12.8

Table 4. Vibrational energies vhv_{vib} (meV) of the D_2 molecule [65] and estimated occupation $P(v)$ of the vibrational quantum levels for two incident beam energies for the hot source in the Cu(001) experiment.

Quantum number v	vhv_{vib} (meV)	$P(v)$[a]	$P(v)$[b]
0	0	0.998	0.990
1	371.32	9.1×10^{-4}	7.0×10^{-3}
2	728.73	2.9×10^{-6}	4.3×10^{-5}
3	1073.13	7.0×10^{-9}	3.0×10^{-7}

[a] $E_i = 200$ meV.
[b] $E_i = 250$ meV.

temperature [61,64]. Once the rotational temperature T_R is determined, rotational populations n_j can be obtained from a Boltzmann distribution.

For the Cu(001) experiment, the values of P_0d used with both sources and the estimated values of T_R are plotted as a function of incident energy in figures 3(a) and (b), respectively. Figures 3(c) and (d) show the populations n_j (expressed in %) of the rotational states with even and odd quantum numbers, respectively, as obtained from a Boltzmann distribution for the rotational temperatures T_R shown in figure 3(b). The discontinuity evident in all the curves of figures 3(b)–(d) at incident beam energies near $E_i \sim 120$ meV was due to the reduction in source pressure in switching from the conventional to the hot source. The pumping speed limitation of P_0 of the latter source decreased the efficiency of the collisional cooling during the expansion. As a consequence, T_R was about a factor 2 higher for the hot source than for the conventional source even when the beam energy was the same. As seen in figure 3(c), for the hot source the population of the $j = 0$ level was less than for the conventional source by almost a factor of 2. This was accompanied by a corresponding increase in the populations of the $j = 2$ and 4 levels. The populations of the odd rotational levels are displayed in figure 3(d). For the experiments on Ni(110), only the conventional source was employed on a limited energy interval. The range of incident energies sampled in the Ni(110) and NiAl(110) experiments was smaller than that in the Cu(001) experiment. Rotational populations calculated with equation (3.2) are reported in table 2 for Ni, and in table 3 for NiAl.

In line with previous experimental work [66,67], we assume that the vibrational population of H_2 and D_2 in a supersonic nozzle beam can be approximated by Boltzmann distributions.

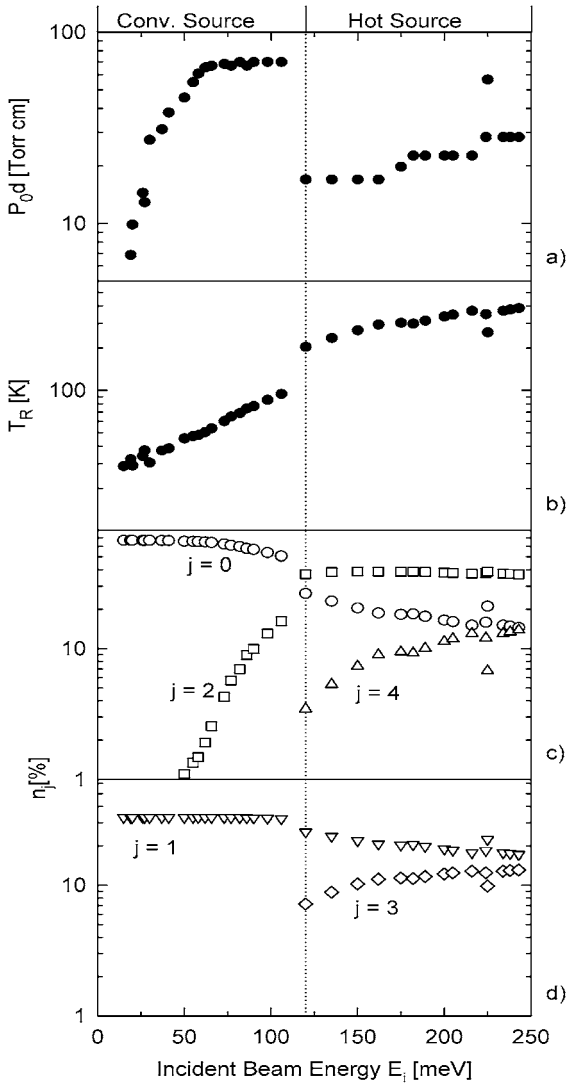

Figure 3. (a) Values of the parameter P_0d used in the D_2/Cu(001) scattering experiments as a function of incident energy. (b) Calculated rotational temperatures T_R corresponding to the source temperature and parameter P_0d employed during the D_2/Cu(001) scattering experiments [64]. (c), (d) Populations n_j of the even (odd) rotational levels as calculated from a Boltzmann distribution with the rotational temperature T_R shown in (b). The vertical dotted line indicates the upper and lower limits of operation with the conventional and the hot sources, respectively.

Table 4 lists the estimated values of the vibrational populations for the hot source in the Cu(001) experiment at two incident energies. Because of the large spacing between the vibrational levels of the D_2 molecule, the occupation of the excited vibrational states is always $<1\%$ for incident energies $E_i \leqslant 250$ meV and can be safely ignored in the analysis of the scattering data.

3.2. Incident beam intensity

To compare diffraction probabilities for He and D_2 from different surfaces and different set-ups, absolute incident beam intensities had to be determined. These measurements are easy in the

Berlin set-up, since the incident beam intensity can be recorded just by removing the sample from the beam and putting the detector behind, but are more complicated for a fixed-angle apparatus. In [24], a procedure was described to determine absolute incident beam intensities in the Göttingen set-up. Here, we describe a simple method to determine relative incident beam intensities. Further details, and a description of supersonic beams, can be found in a review by Pauly [68].

In supersonic nozzle beams the centreline intensity per steradian is given by

$$I(0) = \frac{n_0 \overline{v}}{4\pi} A g(\kappa), \tag{3.3}$$

where n_0 is the number density, $\overline{v}$ the average particle speed, A an effective area proportional to the nozzle diameter, and $g(\kappa)$ is a constant which has a value of 3.473 for monatomic gases and 2.333 for diatomic gases [68]. Simple manipulations show that the beam intensity is proportional to $P_0 d^2 (T_0)^{-1/2}$, where P_0, T_0 are the nozzle pressure and the nozzle temperature, respectively, and d is the nozzle diameter. Two beams produced with the same nozzle at temperatures and pressures $T_{0,1}$, $P_{0,1}$ and $T_{0,2}$, $P_{0,2}$ will have intensities such that

$$\frac{I_1}{I_2} = \frac{P_{0,1}}{P_{0,2}} \frac{T_{0,2}^{1/2}}{T_{0,1}^{1/2}}. \tag{3.4}$$

Equation (3.4) allows us to compare intensities relating to a selected beam nozzle and temperature, and can be employed to determine relative incident beam intensities.

3.3. Diffraction probabilities

Diffraction probabilities $R_{\vec{G}}$ for individual diffraction peaks with reciprocal-lattice vectors $\vec{G}$ were determined with the following procedure. First, the diffraction peak intensities $I_{\vec{G}}$ were determined by fitting Gaussian profiles to the peaks of the angular distributions taken at a given energy and by averaging their integrated intensity over several measurements. In the case of He scattering, $R_{\vec{G}}((\mathrm{He}))$ is obtained by dividing the measured diffraction peak intensities $I_{\vec{G}}(\mathrm{He})$ by the absolute intensity of the He beam incident on the crystal, $I_i(\mathrm{He})$:

$$R_{\vec{G}}(\mathrm{He}) = \frac{I_{\vec{G}}(\mathrm{He})}{I_i(\mathrm{He})}. \tag{3.5}$$

Determination of the D_2 diffraction probabilities requires some additional considerations. It is generally accepted [6, 7, 11, 39] that for chemically inert surfaces the interaction of a molecule with a surface can be separated into the product of a term describing the surface corrugation and another term which accounts for the rotational excitation:

$$V(x, y, z, \Theta) = [V_0(z) + h V_1(z) Q(x, y)](1 + \lambda P_2(\cos\Theta)). \tag{3.6}$$

In equation (3.6), x, y, z describe the position of the molecule in space relative to the surface and Θ is the polar angle of the molecular axis. $V_0(z)$ and $V_1(z)$ are a Morse and an exponential function, respectively, $Q(x, y)$ describes the dependence of the surface corrugation function on x and y, and h is its maximum amplitude. λ is a parameter which describes the anisotropy of a homonuclear molecule and P_2 is the second-order Legendre polynomial.

In a first-order scattering theory this approximation implies that, for a molecule, the sum of the rotationally elastic and inelastic diffraction probabilities equals the diffraction probability for an atom scattered from the same surface. Numerical computations indicate that this separation also holds rather well in higher order [7, 39]. We relied on this approximation to analyse the D_2 data. The diffraction probabilities for D_2 are

$$R_{\vec{G}} = \frac{I_{\vec{G}}(\mathrm{D_2})}{I_i(\mathrm{D_2})}, \tag{3.7}$$

where $I_{\vec{G}}((D_2))$ is the total intensity of diffraction associated with the vector $\vec{G}$:

$$I_{\vec{G}}(D_2) = I_{\vec{G}}^{el} + \sum_{j_i, j_f} \frac{I_{\vec{G}}^{(j_i, j_f)}}{n_{j_i}}. \tag{3.8}$$

In equation (3.8), $I_{\vec{G}}^{el}$ is the intensity of the elastic diffraction peak corresponding to a reciprocal-lattice vector $\vec{G}$ and is assumed to be the same for all rotational states. The quantities $I_{\vec{G}}^{(j_i, j_f)}$ are the RID intensities associated with $\vec{G}$ and the rotational transitions $j = j_i \rightarrow j_f$, and n_{j_i} is the occupation of the rotational level j_i in the incident beam. Division by n_{j_i} is necessary to compare spectra obtained for different nozzle pressures and temperatures (i.e. beams with different rotational populations).

Finally, when comparing He and D_2 intensities, the different ionization cross sections of the two species must be taken into account. This difference is of about a factor two at the electron impact energies of 160 eV employed in the Göttingen set-up [69].

A useful quantity for evaluating RID transition probabilities is the quantity $P^{(j_i, j_f)}$, defined as the ratio of the RID reflectivities for a given rotational transition to the sum of the elastic and inelastic probabilities:

$$P^{(j_i, j_f)} = \frac{\sum_{\vec{G}} R_{\vec{G}}^{(j_i, j_f)}}{\sum_{\vec{G}} R_{\vec{G}}} = \frac{\sum_{\vec{G}} I_{\vec{G}}^{(j_i, j_f)} / n_{j_i}}{\sum_{\vec{G}} I_{\vec{G}}^{el} + \sum_{\vec{G}, j_f} I_{\vec{G}}^{(j_i, j_f)} / n_{j_i}}. \tag{3.9}$$

If effects due to changes in the angles of incidence and Debye–Waller corrections are assumed to be the same for all peaks, $P^{(j_i, j_f)}$ can be looked upon as the relative probability that a molecule incident in the rotational state j_i is inelastically diffracted. Definition (3.9) does not require knowledge of the incident beam intensity, and is particularly useful for a fixed-angle apparatus. In cases where $I_i(D_2)$ can be determined with high accuracy (like with the Berlin set-up), a more conventional expression can be employed to determine rotational transition probabilities:

$$P^{(j_i, j_f)} = \sum_{\vec{G}} \frac{I_{\vec{G}}^{(j_i, j_f)}}{n_{j_i} I_i(D_2)}. \tag{3.10}$$

Definition (3.9) was applied throughout this paper, since fixed- and variable-angle measurements had to be compared.

4. Results and discussion

In this section we focus on the most relevant features of the experimental results. Additional experimental data can be found in [15, 24, 29].

4.1. Measured angular distributions and diffraction probabilities

4.1.1. Cu(001). Figure 4 compares angular distributions of D_2 scattered along the [100] direction of Cu(001) at incident energies between 20 and 250 meV. The surface temperature was $T_s = 60$ K. The angular distributions reported in figure 4(a) were measured with the conventional source, those in figure 4(b) with the hot source. To facilitate comparisons, the intensities of the measurements were arbitrarily normalized to the source pressure and temperature used in the measurement at $E_i = 39$ meV. The intensity of the diffraction peaks was typically more than an order of magnitude smaller than the D_2 specular peak. At the lowest energy of 20 meV only the specular and the lowest-order elastic diffraction peaks were evident.

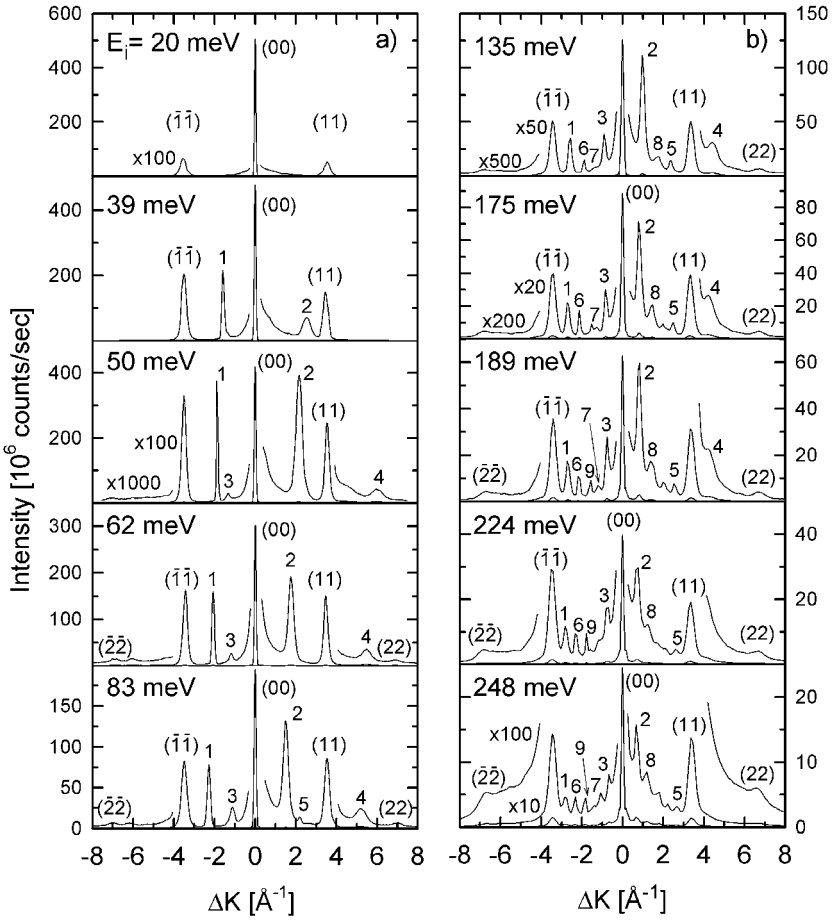

Figure 4. Series of angular distributions of D_2 scattered from Cu(001) along the [100] direction at a surface temperature $T_s = 60$ K. (a) Measured with the conventional source and (b) with the hot source. The numbers label the RID peaks which are identified in table 5.

Several minor peaks and minima are observed for beam energies $E_i < 30$ meV. These have been described and analysed separately [16, 17]. At energies greater than about $E_i = 30$ meV a number of additional peaks, indicated by numbers, were clearly resolved, which are due to RID [24]. The RID peaks in figure 4 were identified using equation (1.1) and were verified with the TOF technique. Table 5 lists the surface reciprocal-lattice vector $\vec{G}$ and the rotational transitions associated with each of the numbered peaks of figure 4. For clarity, only the RID peaks which could be clearly resolved over a significant range of incident energies (at least 50 meV) were considered. Table 5 shows that most RID peaks correspond to the transitions $0 \rightarrow 2$ and $2 \rightarrow 0$ with the smallest energy transfer. These transitions were observed practically over the entire range of incident energies and were the most intense of all the observed inelastic diffraction peaks. Transitions between odd rotational quantum numbers, $1 \rightarrow 3$ and $3 \rightarrow 1$, where the energy transfer is 36.88 meV were observed for incident beam energies E_i greater than about 100 meV, and the rotational transition $2 \rightarrow 4$ with an energy transfer of 51.41 meV was observed only at even larger energies, $E_i > 170$ meV. The multiphonon inelastic background increased steadily at the expense of the diffraction intensities.

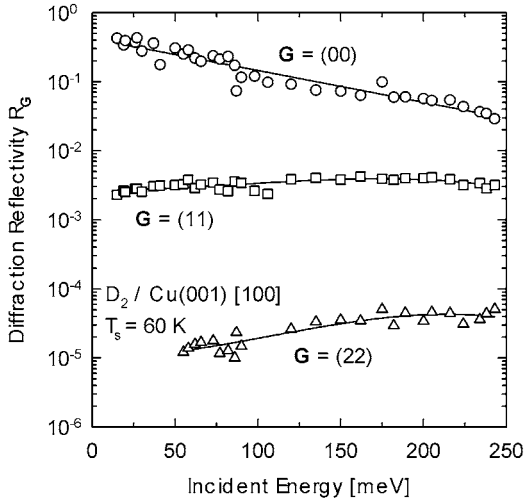

Figure 5. Diffraction probabilities $R_{\vec{G}}$ (equation (3.7)) of D_2 scattered from Cu(001) along the [100] direction at a surface temperature $T_s = 60$ K. Circles: $\vec{G} = (00)$. Squares: $\vec{G} = (11)$. Triangles: $\vec{G} = (22)$. $R_{(11)}$ and $R_{(\bar{1}\,\bar{1})}$ coincided within experimental error, as well as $R_{(22)}$ and $R_{(\bar{2}\,\bar{2})}$. The curves are a guide to the eye.

Table 5. Listing of the surface reciprocal-lattice vectors $\vec{G}$, the rotational transitions $j = j_i \rightarrow j_f$, and the energy transfers ΔE_{rot} corresponding to the observed RID peaks indicated by numbers in figure 4. For clarity, only those peaks which could be clearly resolved over a significant range of incident energies are reported.

Peak No	$\vec{G}$	Transition	ΔE_{rot} (meV)
1	$(\bar{1}\,\bar{1})$	$0 \rightarrow 2$	−22.19
2	(00)	$0 \rightarrow 2$	−22.19
3	(00)	$2 \rightarrow 0$	22.19
4	(11)	$0 \rightarrow 2$	−22.19
5	(11)	$2 \rightarrow 0$	22.19
6	$(\bar{1}\,\bar{1})$	$1 \rightarrow 3$	−36.88
7	(00)	$3 \rightarrow 1$	36.88
8	(00)	$1 \rightarrow 3$	−36.88
9	$(\bar{1}\,\bar{1})$	$2 \rightarrow 4$	−51.41

Starting from the spectra of figure 4, diffraction probabilities can be calculated for all peaks with the method described in section 3.3. We will focus here only on the most relevant quantities: the total diffraction probabilities $R_{\vec{G}}$ defined by equation (3.7). These are reported in figure 5 as a function of incident energy.

In figure 5 the values of $R_{(00)}$ lie on a straight line over the entire range of incident energies. The diffraction probabilities $R_{(11)}$ and $R_{(\bar{1}\,\bar{1})}$ were found to coincide within error over the whole range of incident energies covered by the experiment. In the following, both $R_{(11)}$ and $R_{(\bar{1}\,\bar{1})}$ are referred to as $R_{(11)}$. $R_{(11)}$ remains approximately constant between 50 and 250 meV which indicates that the increase in diffraction probability with greater incident energy compensates for the Debye–Waller attenuation of the intensity with increasing incident energy. The fourth-order diffraction probabilities, $R_{(22)}$, show a similar trend as a function of the incident energy as $R_{(11)}$ over the range of energies where they could be detected.

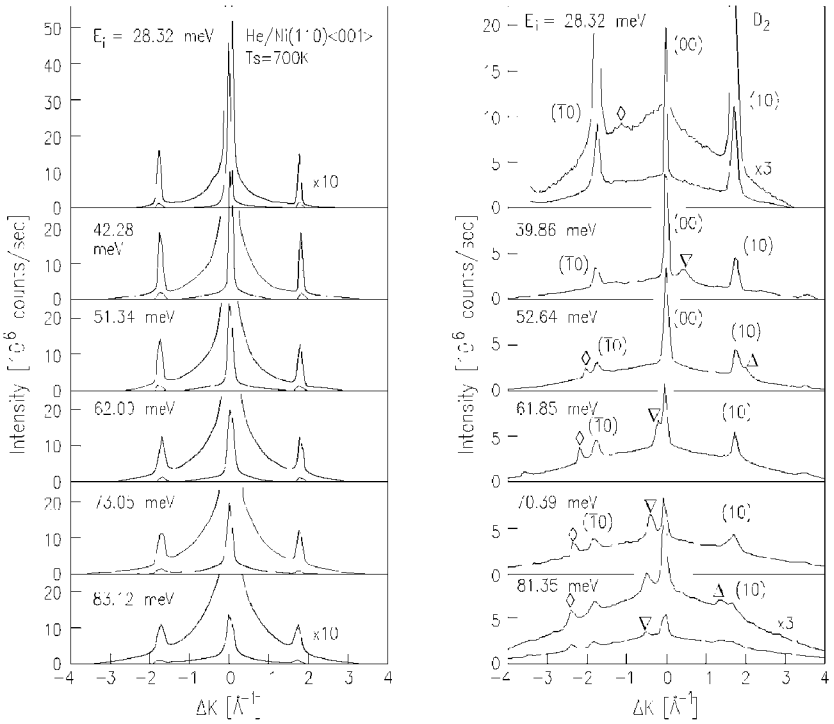

Figure 6. Comparison of angular distributions of He (a) and of D_2 (b) scattered from Ni(110) along the [100] direction at different incident energies. The surface temperature in both measurements was $T_s = 700$ K. To facilitate a direct comparison, the intensities in each of the frames have been corrected so that they correspond to the same incident beam flux as was used in the measurement for He at $E_i = 42.28$ meV. The symbols correspond to RID peaks. Diamonds: $j = 0 \rightarrow 2$, $\vec{G} = (\bar{2}0)$. Inverted triangles: $j = 0 \rightarrow 2$, $\vec{G} = (\bar{1}0)$. Triangles: $j = 0 \rightarrow 2$, $\vec{G} = (00)$. The shift from left to right of the position of the RID peaks is in accordance with equation (1.1).

4.1.2. Ni(110). Figure 6 compares six typical angular distributions taken along the [001] direction for He and D_2 at beam energies between 28 and 84 meV. The measurements were performed along the [001] direction (perpendicular to the rows) where the diffraction peaks were more intense due to the higher corrugation. Measurements along the less corrugated $[1\bar{1}0]$ direction showed diffraction peaks which were more than a factor 2 less intense than along the [001] direction and could not be distinguished from the multiphonon background for incident energies $E_i > 70$ meV.

For a more direct comparison, the intensities of both the He and D_2 series of measurements were normalized to the same source conditions of pressure and temperature so that the incident beam fluxes were the same as in the measurement for He at $E_i = 42.28$ meV and $T_s = 700$ K.

The most striking difference between the two sets of angular distributions is the large difference in the specular signals, the D_2 signal being smaller by about a factor of 200 at an incident energy $E_i = 28$ meV. The first-order diffraction intensities relating to the specular peak appear to be quite different for the two systems, those for D_2 being approximately a factor of 7 larger than those for He. Three RID peaks could be resolved, which corresponded to the $0 \rightarrow 2$ transition and were coupled to the three surface reciprocal-lattice vectors $\vec{G} = (\bar{2}0)$, $(\bar{1}0)$, (00).

Figure 7 displays diffraction probabilities $R_{\vec{G}}$ for He and D_2 as a function of incident energy. The values of $R_{(00)}$(He) are more than one order of magnitude larger than those

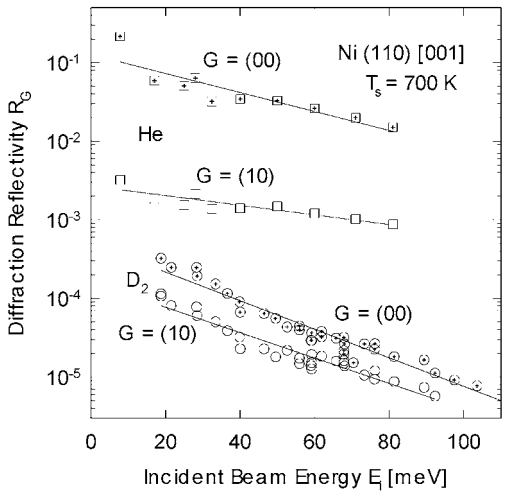

Figure 7. Diffraction probabilities $R_{\vec{G}}$ (equation (3.7)) of He and D_2 scattered from Ni(110) [001] at a surface temperature $T_s = 700$ K. Squares: He; circles: D_2. The lines are a guide to the eye.

of $R_{(10)}$(He), since the intensities of the He diffraction from low-index metal surfaces are typically <1% of the specular peak. For D_2, only negligible or extremely weak RID peaks were observed at energies $E_i \leqslant 40$ meV, and these peaks were neglected when calculating $R_{(00)}(D_2)$. In the energy range $45 \leqslant E_i \leqslant 65$ meV the RID peak associated with $\vec{G} = (00)$ could not be resolved from the elastic diffraction peak associated with $\vec{G} = (\bar{1}0)$ (see also figure 4). Finally, for incident energies $E_i > 93$ meV the zero-order RID peak disappears in the multiphonon background.

The diffraction probabilities for He and D_2 decrease exponentially over the entire range of incident energies, the values for the D_2 diffraction probability being typically 0.5% of the He values. This exponential decrease can be interpreted as due to a Debye–Waller attenuation.

4.1.3. NiAl(110). Figure 8 shows a series of angular distributions of D_2 scattered from NiAl(110) at incident energies between 88 and 157 meV. The incident beam was along the $[1\bar{1}0]$ direction of the surface, which was kept at 90 K during the measurements. The first thing to notice in comparison with the Cu(001) and Ni(110) spectra shown above is the large intensity scattered into the first-order diffraction beams, which are typically only a factor of 5 less intense than the specular beams. This is a consequence of the larger corrugation of this surface, and was also observed with He and Ne diffraction [28]. Two RID peaks are also clearly visible for all incident energies. From the position of these peaks and the equations for the conservation of energy and parallel momentum (1.1), the RID peaks could be identified as corresponding to the transitions $0 \rightarrow 2$ (coupled to $\vec{G} = (0\bar{1})$) and $2 \rightarrow 0$ (coupled to $\vec{G} = (01)$).

Absolute diffraction probabilities $R_{\vec{G}}$ as defined by (3.7) are plotted in figure 9 as a function of incident energy. Similarly to the case for Cu(001), the ratio of the diffraction peaks to the specular ones decreases with increasing incident energy, indicating that a larger corrugation amplitude is sampled by the incident beam. Note also the change in the slope of the (00) beam at $E_i \sim 120$ meV, which suggests a change in the Debye–Waller behaviour, as discussed in more detail below.

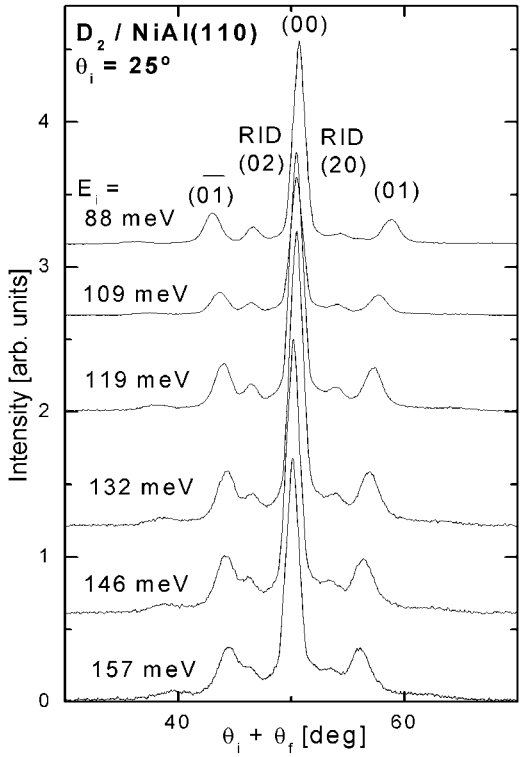

Figure 8. A series of angular distributions of D_2 incident along the $[1\bar{1}0]$ direction of NiAl(110), at a surface temperature $T_s = 90$ K.

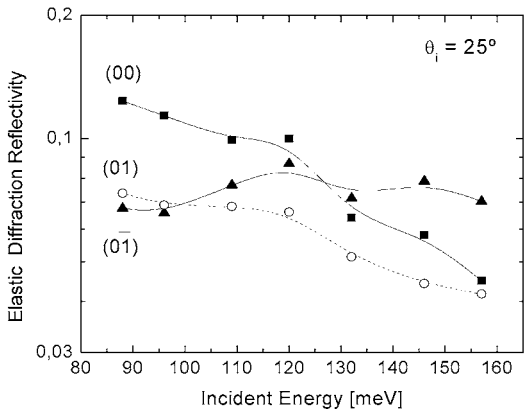

Figure 9. Diffraction probabilities $R_{\vec{G}}$ of D_2 scattered from NiAl(110) along the $[1\bar{1}0]$ direction at a surface temperature $T_s = 90$ K. The angle of incidence was $\theta_i = 25^\circ$. Squares: $\vec{G} = (00)$; circles: $\vec{G} = (01)$; triangles: $\vec{G} = (0\bar{1})$. The curves are a guide to the eye.

4.2. Debye–Waller analysis

To compare experiment and theory, the attenuation of diffraction intensities with surface temperature and incident beam energy must be accounted for. A standard method is to use a

Debye–Waller model. In a Debye–Waller analysis, the intensity $I_{\vec{k}}(T_s)$ of a diffraction peak with momentum transfer $\hbar\vec{k} = \hbar(\vec{k}_i - \vec{k}_f)$ at a crystal temperature T_s is given by

$$I_{\vec{k}}(T_s) = I_{\vec{k}}(0)\mathrm{e}^{-2W(T_s)}, \tag{4.1}$$

where $I_{\vec{k}}(0)$ is the diffracted intensity at 0 K surface temperature. $W(T_s)$ is the Debye–Waller exponent which can be approximated by [70, 71]

$$W(T_s) = \frac{3\hbar^2(k'_{iz} + k'_{fz})^2 T_s}{2Mk_B\theta_D^2}, \tag{4.2}$$

M being the mass of a surface atom, k_B the Boltzmann constant, and θ_D the surface Debye temperature. k'_{i_z} and k'_{f_z} are the normal components of the incident and scattered wavevectors, respectively, corrected for the potential well depth (Beeby correction) [72]:

$$k'_{i\,(f)z} = \sqrt{k^2_{i\,(f)z} + 2m\epsilon/\hbar^2}, \tag{4.3}$$

ϵ being the potential well depth and $k_{i\,(f)z}$ the normal component of the incident (scattered) wavevector. For the specular beam, (4.2) can be easily expressed as a function of the incident beam energy E_i and the angle of incidence θ_i:

$$W(T) = \frac{12m(E_i\cos^2\theta_i + \epsilon)T}{Mk_B\theta_D^2}. \tag{4.4}$$

The attenuation predicted by the Debye–Waller model does not always agree with experiment in both the momentum *and* the temperature dependences [2]. We will show, however, that a Debye–Waller model reproduces reasonably well the data in the range of energies and surface temperatures considered in our experiments.

4.2.1. Cu(001). The attenuation of the diffraction intensities with surface temperature was measured for incident energies between $E_i = 100$ and 250 meV, and the data are reported in figure 10. Due to the high incident energies, the increase of the multiphonon background with surface temperature was extremely high. Most diffraction peaks were already unresolvable at $T_s = 100$ K and the data of figure 10 relate only to the most intensive diffraction peaks, $I^{el}_{(00)}$, $I^{el}_{(11)}$, $I^{(0,2)}_{(\bar{1}\bar{1})}$, and $I^{(0,2)}_{(00)}$. To account for the Beeby correction, equation (4.3), a value $\epsilon = 32.3$ meV of the potential well depth was assumed as determined in recent experimental measurements [16, 17]. This value is very close to the value $\epsilon = 30.9$ meV determined by Andersson and co-workers [18] and is significantly larger than the value $\epsilon = 22.3$ meV previously reported by Lapujoulade and Perreau (LP) [14]. The best fit of equation (4.2) to the data of figure 10 yields a surface Debye temperature of $\theta_D = 341 \pm 30$ K which does not depend on incident energy. This value for the surface Debye temperature is higher than the values $\theta_D = 270$ K determined by recent He scattering measurements for Cu(001) [51] and $\theta_D = 302$ K (including $\epsilon = 5.7$ meV) reported by Goncharova *et al* [13]. However, it agrees reasonably well with the value $\theta_D = 373$ K determined by Lapujoulade and Perreau [14] in previous measurements on H_2 scattered from Cu(001). We mention for completeness that a surface Debye temperature of $\theta_D = 299$ K (with $\epsilon = 30.5$ meV) has recently been reported for HD scattering from Cu(001) in [13].

4.2.2. Ni(110). The diffraction peak intensities were also investigated as a function of surface temperature on Ni(110) and are reported in figure 11.

From the attenuation of the He specular peak, and assuming a value $\epsilon = 5$ meV for the potential well depth [25], the surface Debye temperature is $\theta_D = 374 \pm 12$ K. This result lies within

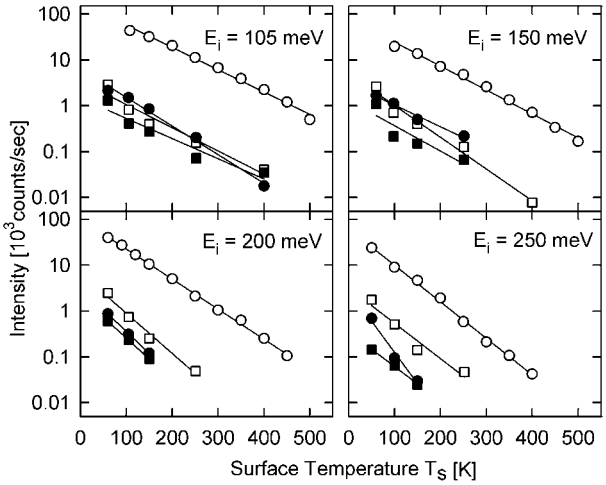

Figure 10. Debye–Waller attenuation of diffraction intensities in the D_2/Cu(001) experiment at the indicated energies. Circles: $I^{el}_{(00)}$; squares: $I^{el}_{(11)}$; filled circles: $I^{0,2}_{(00)}$; filled squares: $I^{0,2}_{(\bar{1}\bar{1})}$. The lines are best fits of equation (4.1) to the experimental data.

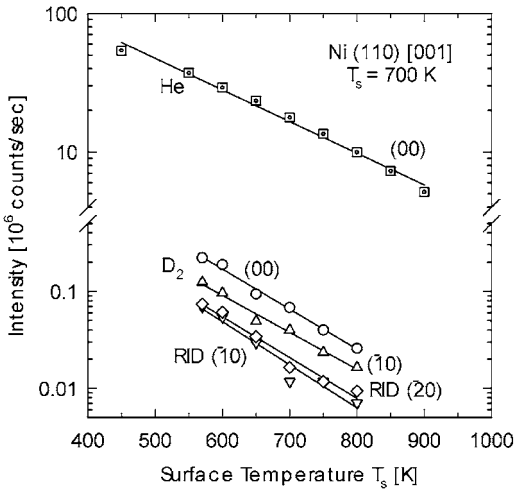

Figure 11. Debye–Waller attenuation of diffraction intensities in the Ni(110) experiment. The incident energy was $E_i = 75.50$ meV for He and $E_i = 67.80$ meV for D_2. Squares: I_{00}(He); circles: $I^{el}_{00}(D_2)$; triangles: $I^{el}_{\bar{1}0}(D_2)$; diamonds: $I^{0,2}_{\bar{2}0}(D_2)$; inverted triangles: $I^{0,2}_{\bar{G}=(\bar{1}0)}(D_2)$. The lines are best fits of equation (4.1) to the experimental data.

the range reported in the literature which extends from $\theta_D = 286$ K measured using LEED by Andersson and Kus [73] on a Ni(001) surface and $\theta_D = 300$ K, obtained for a Ni(110) surface by Liebsch and Harris [74] from an analysis of the experimental data of [25], up to the value $\theta_D = 595$ K measured using He scattering by Hayward and Taylor [23] for the Ni(001) surface.

For D_2, a Debye temperature of $\theta_D = 387 \pm 12$ K close to the above value for He is obtained when a value $\epsilon = 45$ meV for the potential well depth is assumed. This well depth is consistent with the value resulting from the eikonal fit to the D_2 diffraction data. Our value is greater than the value $\epsilon = 25$ meV frequently assumed [23, 75], and somewhat greater than values reported for similar surfaces.

The attenuations of the diffraction probabilities with incident energy observed in figures 5 and 7 are also related to a Debye–Waller attenuation. Fits to the data of figure 7 yield Debye temperatures of 460 K for He and 373 K for D_2, in fair agreement with the values obtained from the fit to the data of figure 11. Our conclusion is apparently at odds with theoretical and experimental evidence. Simulations of H_2 dissociation on Pd(001) showed that diffraction probabilities decreased with increasing incident energy even for a frozen surface [76]. This was interpreted as an increase of dissociative chemisorption probability with increasing incident energy. In our Ni(110) experiments, the diffraction probabilities decrease by about a factor 15 for energies between 20 and 100 meV. In the same energy interval, theory predicts a decrease of only about a factor 2. A decrease in coherent scattering probability induced by an increase of dissociative chemisorption cannot be ruled out, but it is probably overshadowed by the much larger Debye–Waller attenuation. Also, measurements of H_2 scattered from Pd(001) and Cu(001) have shown that rotational excitation probabilities increase with increasing temperature at low incident energies [77–79]. In our experiments, RID probabilities decrease when temperature is increased. These observations can be reconciled, since the measurements of [77–79] refer to the overall scattering probability, i.e., molecules scattered coherently and incoherently. Diffraction measurements probe only the coherently scattered fraction, which is extremely sensitive to surface vibrations. The apparent discrepancy with theoretical and experimental results suggests, however, that a more systematic analysis of RID as a function of surface temperature may yield more than (yet another) value of the surface Debye temperature.

4.2.3. NiAl(110). The Debye–Waller attenuation of the specular beam for the scattering of He and D_2 from NiAl(110) is shown in figure 12 as a function of surface temperature and incident beam energy. The surface temperature dependence was verified for two different angles of incidence. The dependence on perpendicular momentum transfer was tested by plotting data recorded at different incident energies and angles of incidence. The solid lines are best fits to the data points using (4.4) and $M = 27$ (corresponding to the mass of aluminium, the topmost atoms on this surface). The best-fit parameters are: $\theta_D = 830 \pm 45$ K and $\epsilon = 7$ meV for He; and $\theta_D = 823 \pm 43$ K and $\epsilon = 35$ meV for D_2. We also mention that in the case of D_2, the Debye–Waller behaviour was verified as a function of incident energy only for values up to 120 meV, and that the specular intensity was found to decrease much faster at larger E_i-values [29]. The origin of this behaviour may be in the larger corrugation of this surface, which makes the range of validity of the approximations implicit in (4.4) very narrow.

In summary, the results obtained for the Debye–Waller analysis of Cu(001) and Ni(110) are in substantial agreement with previous results and the overall trends for scattering of hydrogen from single-crystal surfaces. The results for NiAl(110), however, suggest that this model works on this particular surface only for incident energies below about 100 meV.

4.3. Eikonal approximation: applications and limitations

The eikonal approximation is a simple theoretical method that can be employed to analyse diffraction intensities of atoms and molecules scattered from rigid surfaces with small corrugation [80]. While we are well aware of the limitations of this approximation, it has the advantage of simplicity, and it has proven to be quantitatively correct for small values of the corrugation amplitude and for scattering at small angles [2].

In the eikonal approximation, the interaction potential is approximated by a hard wall with a corrugation modelled—in the case of a square lattice like Cu(001)—by the function [14,80,81]:

$$\zeta(x, y) = \frac{h}{2}\left[\cos\left(\frac{2\pi}{a}x\right) + \cos\left(\frac{2\pi}{a}y\right)\right], \tag{4.5}$$

where h is the corrugation amplitude, a the lattice constant, x and y the symmetry directions of the surface lattice. When equation (4.5) is used to model the surface corrugation profile, the eikonal diffraction probabilities can be expressed analytically [6]:

$$P_{\vec{G}} = \frac{k_{fz}}{k_{iz}} J^2_{|m|}\left(\frac{h}{2}\Delta k'_z\right) J^2_{|n|}\left(\frac{h}{2}\Delta k'_z\right), \tag{4.6}$$

where $P_{\vec{G}}$ is the diffraction probability of the peak coupled to the surface reciprocal-lattice vector $\vec{G} = (m, n)$ (m and n integers), and $J_{|m|}(x)$ and $J_{|n|}(x)$ are the Bessel functions of order $|m|$ and $|n|$. $\Delta k'_z = k'_{f_z} - k'_{i_z}$ is the difference between the normal components of the incident and scattered wavevectors. The diffraction probabilities at finite temperatures are obtained by multiplying equation (4.6) by the Debye–Waller attenuation, equation (4.1).

The eikonal approximation can also be extended to the case of RID to predict RID probabilities [6]. In this model, a homonuclear diatomic molecule is approximated by a prolate ellipsoid with eccentricity δ and principal axes b and $b(1-\delta^2)^{-1/2}$. The diffraction probability of a RID peak coupled with a vector $\vec{G}$ and the transition $j_i \to j_f$ is given analytically by

$$\begin{aligned} P_{\vec{G}}^{(j_i, j_f)} = {} & \frac{1}{120} b^2 \delta^4 \frac{(2j_f+1)(j_f+j_i)(j_f+j_i+2)}{(j_f+j_i-1)(j_f+j_i+1)(j_f+j_i+3)} \frac{k_{fjz}}{|k_{iz}|} \\ & \times \left\{ \left[|k'_{iz}| J_{|m|}\left(\frac{h}{2}\Delta k'_{jz}\right) J_{|n|}\left(\frac{h}{2}\Delta k'_{jz}\right) + k'_{fz} J_{|m|}\left(\frac{h}{2}\Delta k'_z\right) J_{|n|}\left(\frac{h}{2}\Delta k'_z\right) \right]^2 \right. \\ & \left. + \frac{12\pi^2}{a^2}(m^2+n^2)\frac{k^2_{iz}}{\Delta k'_{jz}} J^2_{|m|}\left(\frac{h}{2}\Delta k'_{jz}\right) J^2_{|n|}\left(\frac{h}{2}\Delta k'_{jz}\right) \right\}. \end{aligned} \tag{4.7}$$

In equation (4.7), k'_{fjz} is the perpendicular component of the RID peak scattered wavevector, $\Delta k'_{jz} = k'_{fjz} - k'_{iz}$, and the other symbols have the same meaning as in equation (4.6), the Beeby correction being taken into account in the perpendicular components of the wavevectors. The diffraction probabilities at finite temperatures are accounted for as in the case of elastic diffraction by multiplying equation (4.7) by the Debye–Waller exponent.

4.3.1. Cu(001). Figure 13 shows, as a function of incident energy, the ratios of $R_{(11)}/R_{(00)}$ and $R_{(22)}/R_{(00)}$, respectively. Plotting and fitting these ratios instead of absolute probabilities has the advantage of getting rid of some of the flux issues described in section 3. The curves show a nearly exponential increase with incident energy. The curves in figure 13 represent the results of the eikonal best fit to the experimental data. The best fit to the data was obtained with a corrugation amplitude $h = 0.075 \pm 0.08$ Å, independent of incident energy. This value of the corrugation amplitude is larger than the value $h = 0.061$ Å reported in [14] and is probably due to differences in the Debye temperatures and potential well depth used in the calculations of [14].

4.3.2. Ni(110). Figure 14 shows, as a function of incident energy, the ratios $R_{(10)}/R_{(00)}$ for He and D_2. The D_2 experimental points between 45 and 65 meV have been omitted since one RID peak nearly coincided with the specular peak in that energy range, and made intensity calculations nearly impossible. At the higher incident energies the error bars of the D_2 data are significantly greater than those for He because of the increased inelastic background.

The best fit of the eikonal theory to the He data is shown by the continuous line, and was obtained using a one-dimensional corrugation with an amplitude $h = 0.06 \pm 0.005$ Å and a potential well depth $\epsilon = 4 \pm 2$ meV. The corrugation amplitude is in reasonable agreement with the value of 0.05 Å reported by Engel and Rieder [25] for the same system. Also, no dependency of the corrugation amplitude on the incident energy was required to fit the

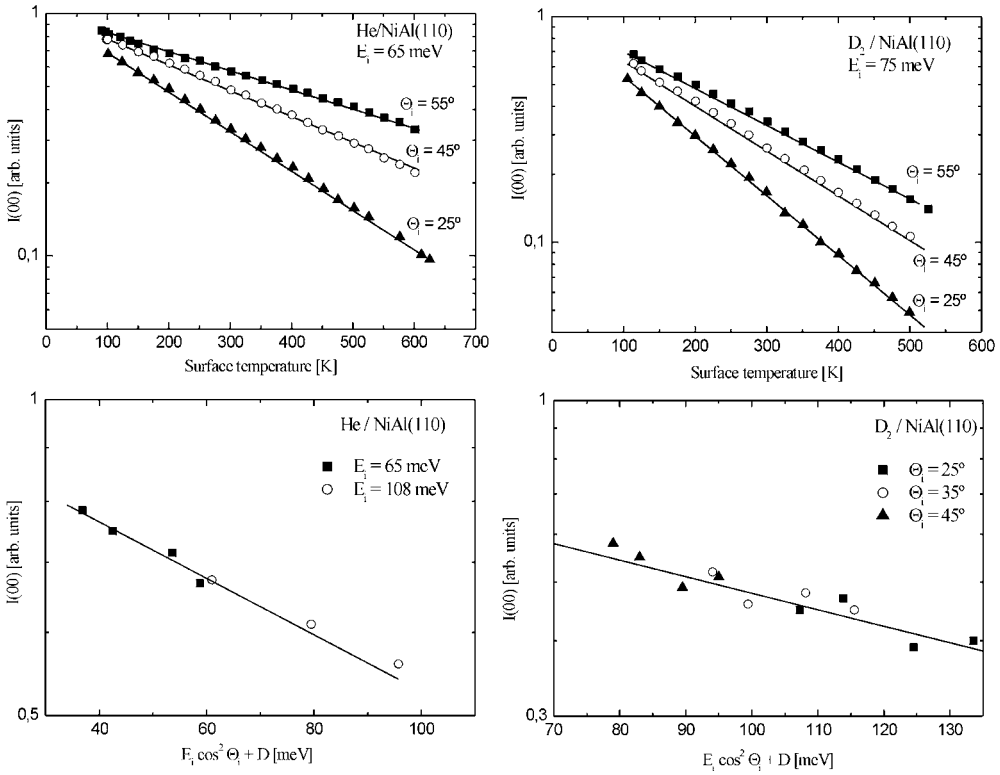

Figure 12. Debye–Waller attenuation of specular diffraction intensity for the scattering of He and D_2 from NiAl(110) as a function of surface temperature and incident beam energy for two different angles of incidence. The lines are best fits of (4.4) to the experimental data.

data, in accordance with previous analysis by Engel and Rieder in a similar range of incident energies [25] and with that of García *et al* [82]. The same corrugation function was also used to fit the D_2 diffraction data. The best-fit values are $h = 0.091 \pm 0.01$ Å for the corrugation amplitude, and $\epsilon = 45 \pm 7$ meV for the potential well depth. The results are shown by the dashed line in figure 14. Also in this case a good fit could be obtained without including an energy dependence of the corrugation amplitude.

4.3.3. NiAl(110). A preliminary analysis on NiAl(110) shows that the eikonal approximation does not describe properly D_2 diffraction over a large range of incident energies from this surface. A fit was possible only for incident energies of 70–80 meV and yielded a value $h = 0.12$ Å of the corrugation amplitude [28, 29]. The limited range of applicability of the eikonal approximation is probably due to the large corrugation amplitude of this surface.

4.4. Rotationally inelastic diffraction (RID)

A striking result of our measurements is the observation of a large number of RID peaks. Except for in a few experiments [31], diffraction of the highly symmetric H_2 and D_2 molecules from metallic surfaces showed RID peaks only as weak shoulders of the elastic diffraction peaks [4, 9, 14, 20, 26, 84]. This difference is probably due to the higher angular and energy resolution of the present experiments. The RID peaks are often in the immediate neighbourhood

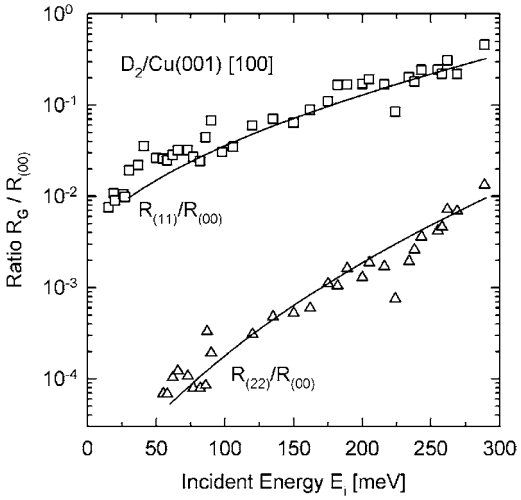

Figure 13. The ratio between diffraction probabilities of D_2 scattered from Cu(001) [100] at a surface temperature $T_s = 60$ K. Squares: $R_{(11)}/R_{(00)}$; triangles: $R_{(22)}/R_{(00)}$. The solid curves indicate the eikonal fit to the data with a value of the corrugation amplitude $h = 0.075$ Å and a potential well depth $\epsilon = 32.3$ meV.

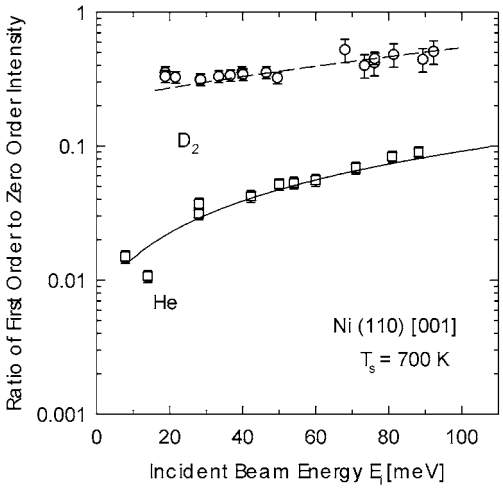

Figure 14. The ratio between first-order and zero-order diffraction probabilities for He (squares) and D_2 (circles) scattered from Ni(110) [100]. The surface temperature is $T_s = 700$ K. The solid curve is the eikonal fit to the He data with a corrugation amplitude $h = 0.06$ Å and a potential well depth $\epsilon = 4$ meV. The dashed curve is the eikonal fit to the D_2 data with a corrugation amplitude $h = 0.091$ Å and a potential well depth $\epsilon = 45$ meV.

of elastic diffraction peaks, and a very high angular and energy resolution is required to clearly distinguish the different contributions. Also, most previous experiments had been carried out at relatively low incident energies $E_i \leqslant 100$ meV and with the lighter H_2 molecules for which the lowest transition ($0 \rightarrow 2$) has an energy transfer $\Delta E_{rot} = -43.93$ meV. In the present experiments the higher incident energies $E_i > 100$ meV made it possible to clearly resolve the RID peaks coupled to the rotational transitions with lowest energy transfer ($0 \rightarrow 2$ and $2 \rightarrow 0$,

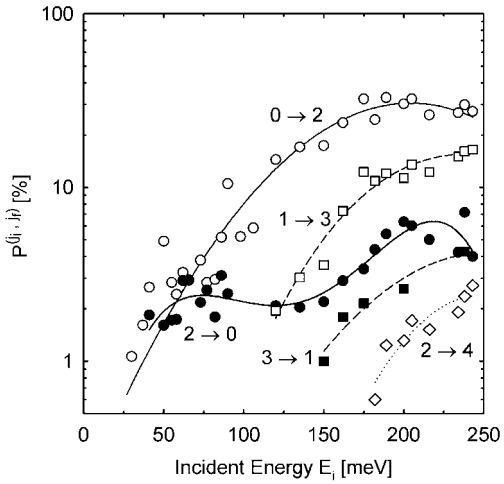

Figure 15. Rotational inelastic transition probabilities P^{j_i,j_f}, equation (3.9). Circles: $0 \rightarrow 2$; filled circles: $2 \rightarrow 0$; squares: $1 \rightarrow 3$; filled squares: $3 \rightarrow 1$; diamonds: $2 \rightarrow 4$. The curves are guides to the eye. The D_2 beam was incident along the [100] direction of Cu(001), the surface temperature was $T_s = 60$ K.

$|\Delta E_{rot}| = 22.37$ meV), but also the $1 \rightarrow 3$, $3 \rightarrow 1$, and $2 \rightarrow 4$ transitions, where the energy transfer ($|\Delta E_{rot}| = 36.88$ and 51.41 meV, respectively) is comparable to that of H_2 molecules.

4.4.1. Cu(001). A qualitative gauge of rotationally inelastic transition probabilities is represented by the quantity $P^{(j_i,j_f)}$ defined in (3.9), and plotted in figure 15 as a function of incident energy. The scatter in the data arises largely from the cumulative errors in the input data and the numerous corrections to the experimental data[4]. $P^{(j_i,j_f)}$ increases for all transitions (except $2 \rightarrow 0$) by about a factor 10 when the energy increases from $E_i \approx 50$ to about 200 meV. The $0 \rightarrow 2$ transition has the highest probability and represents more than 30% of the elastic scattering probability along the [100] direction at energies larger than 150 meV. This high value of the rotational transition probability may appear surprising in view of previous experimental results, and constitutes one of the major findings of our experiment.

To gain a better insight in the RID, the RID probabilities of figure 15 were analysed with the eikonal approximation. In the calculations, the corrugation was kept fixed at the value $h = 0.075$ Å determined from the fit to the data of figure 13. The parameter b in equation (4.7) was also fixed at the value $b = 1.48$ Å, in accordance with previous work [65, 85, 86]. The eccentricity parameter was varied between $\delta = 0.3$ and 0.5, which represent the limits indicated by previous theoretical work [85,86]. Table 6 compares the experimental data taken at energies $E_i = 200$ and 250 meV with the results of the theoretical calculations obtained for $\delta = 0.3$ and 0.4, respectively. The value $\delta = 0.4$ was used in the past by Levi and co-workers [6] as an average value for the H_2 molecule to show that their theoretical approach could qualitatively account for measured RID intensities [20]. The best agreement with our experimental data is obtained with $\delta = 0.3$.

In view of the simplicity of the theory and of the rather large uncertainties in the experimental data the agreement between the calculated and the measured values is rather

[4] The errors originate in part from the approximations used for the determination of the incident D_2 beam flux, and partly from the procedure employed in section 3.1 for the determination of the rotational populations of the incident beam.

Table 6. Comparison of the experimental and theoretical values of the rotationally inelastic transition probability $P^{(j_i,j_f)}$. The uncertainty of the experimental data is estimated to be ±20%.

	$E_i = 200$ meV			$E_i = 250$ meV		
		Theory			Theory	
Transition	Experiment	$\delta = 0.3$	$\delta = 0.4$	Experiment	$\delta = 0.3$	$\delta = 0.4$
$0 \to 2$	0.30	0.25	0.52	0.25	0.28	0.51
$2 \to 0$	0.07	0.06	0.16	0.03	0.07	0.19
$1 \to 3$	0.11	0.16	0.39	0.15	0.19	0.43
$3 \to 1$	0.03	0.07	0.20	0.03	0.09	0.23
$2 \to 4$	0.01	0.05	0.09	0.04	0.09	0.14

satisfactory. We interpret this result as indicating that the rotational transition probability can be accounted for by a hard-wall-type interaction. We also point out that the low probability of the $2 \to 0$ and $3 \to 1$ de-excitation transitions is correctly accounted for by the theoretical model. This result can be understood by taking the limit of equation (4.7) at high incident energies. At high incident energies the wavevectors appearing in equation (4.7) are constants, and the main difference between the excitation and de-excitation probabilities is given by the factor multiplying the parentheses on the left side. We can then write

$$\frac{P_{\vec{G}}^{(j_i,j_f)}}{P_{\vec{G}}^{(j_f,j_i)}} \approx \frac{(2j_f+1)}{(2j_i+1)} = \begin{cases} 5 & \text{for } j_i = 0,\ j_f = 2 \\ 7/3 & \text{for } j_i = 1,\ j_f = 3. \end{cases} \tag{4.8}$$

The success of (4.8) in predicting the trends at high energies is not accidental. Equation (4.8) is intimately bound to the principle of detailed balancing. According to detailed balancing, the direct ($R^{(i,f)}$) and reverse ($R^{(f,i)}$) probabilities for a rotational transition $j_i \to j_f$ are coupled by the relation [87]

$$\frac{R^{(i,f)}}{g_f E_f} = \frac{R^{(f,i)}}{g_i E_i}, \tag{4.9}$$

$g_{f\,(i)}$ being the density of levels of the final (initial) level $f\,(i)$ and $E_{f\,(i)}$ the kinetic energy after (before) collision. In the limit of high energies, the rotational transition energy is negligible, $E_f \approx E_i$, and (4.8) is obtained.

4.4.2. Ni(110). The quantity $P^{(j_i,j_f)}$ is plotted in figure 16 for D_2/Ni(110) as a function of incident energy. Due to the high inelastic background, only three RID peaks were resolved for scattering of D_2 from Ni(110). Compared to the case for Cu(001), the RID transition probability is much higher, and represents up to 50% of the total diffracted intensity. A fit to the data of figure 16 with the eikonal approximation, equation (4.7), was attempted. Contrary to the case for Cu(001), a satisfactory fit could only be obtained by increasing the value of the corrugation amplitude by more than 50% from the value obtained fitting equation (4.6) to the total diffraction probabilities of figure 14.

There are at least two reasons for the discrepancy between the fit to the total diffraction and the RID probabilities. In the first place, the eikonal approximation for rotations, equation (4.7), assumes the rotational transition probabilities to be small, which is not the case for Ni(110). Secondly, the scattering potential is highly anisotropic in the orientation of the molecular axis, and this favours rotational excitation, as discussed in [88]. The overall scattering potential probably remains separable, and equation (4.6) works well for fitting the data of figure 14, but the RID probabilities are strongly enhanced, and cannot be accounted for by equation (4.7).

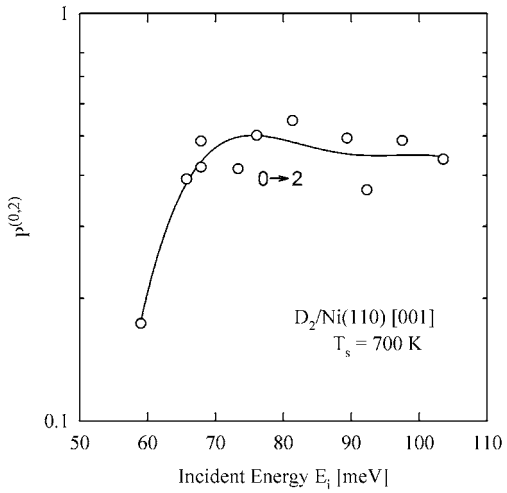

Figure 16. Rotational inelastic transition probabilities $P^{(0,2)}$, equation (3.9). The D_2 beam was incident along the [001] direction of Ni(110); the surface temperature was $T_s = 700$ K. The curves are a guide to the eye.

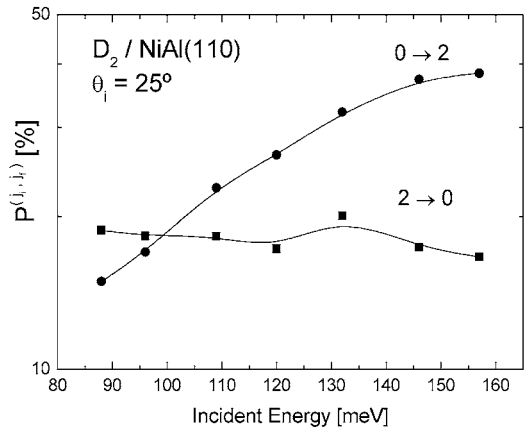

Figure 17. Rotational inelastic transition probabilities $P^{(0,2)}$ and $P^{(2,0)}$ as defined by (3.10). The D_2 beam was incident along the [001] direction of NiAl(110). The curves are a guide to the eye.

4.4.3. NiAl(110). Figure 17 shows a plot of $P^{(0,2)}$ and $P^{(2,0)}$ defined by (3.9) as a function of incident energy for a D_2 beam incident along the $[1\bar{1}0]$ direction of NiAl(110). All data points were recorded at the same angle of incidence $\theta_i = 25^\circ$. The $P^{(0,2)}$-probability increases with incident energy. For an energy of about 100 meV, the $0 \rightarrow 2$ transition probability for NiAl(110) is about a factor 2 lower than on Ni(110), and about a factor 2 higher than on Cu(001). While the difference between the NiAl and Cu cases is probably due to the larger corrugation amplitude of NiAl, the same argument does not hold for Ni(110), whose corrugation is smaller than NiAl (see table 1).

The high rotational transition probabilities on Ni(110) are probably related to the angular anisotropy of the dissociative chemisorption potential. The most favourable orientation for dissociation of hydrogen on surfaces is when the molecular axis is parallel to the surface. Molecules whose axis is not parallel to the surface will be steered into the more favourable

configuration, i.e., forced to rotate [83]. Simulations of hydrogen scattering from Pd(001) [76] and from Cu(111) [88] for energies higher than the activation barrier show also rotational transition probabilities as high as 50%, in qualitative agreement with our experiments. Comparison with results of other molecular scattering experiments also shows that high rotational excitation probabilities are common for non-activated systems. For example, rotational transition probabilities are much higher for scattering of HD from Ni(001) than from Cu(001) [12, 13].

5. Conclusions

We have measured D_2 diffraction from three single-crystal surfaces that represent the prototypes of a system with a high barrier to dissociative chemisorption, Cu(001), low or vanishing barrier, Ni(110), and an alloy surface with a high activation barrier, NiAl(110). Diffraction spectra from all surfaces exhibit both elastic and rotationally inelastic peaks.

Attenuation of the diffraction peaks with surface temperature and incident energy was found in fair agreement with a simple Debye–Waller model, at least for the range of incident energies and angles considered by our experiments.

Fits of the diffraction probabilities with the eikonal approximation were attempted for all systems, but were found to be in good agreement with experiment only for the high-barrier, low-corrugation system Cu(001). Dissociative chemisorption on Ni(110) and the large geometric corrugation of NiAl(110) modify the scattering potential in such a way that the eikonal approximation cannot be applied.

The most important result of our experiments is the measurement of a large number of rotational transition peaks. This allowed us to determine rotational transition probabilities. The probability of rotationally inelastic transitions, in general, increases with incident energy. For a same energy, the rotational excitation probability is higher for the low-barrier system Ni(110) than for the high-barrier Cu(001) and NiAl(110) surfaces. The high rotational transition probability measured for Ni(110) is qualitatively in agreement with previous simulations of hydrogen scattering off Pd(001) and Cu(111) for energies higher than the activation barrier, and is attributed to the angular anisotropy of the dissociative chemisorption potential. The most favourable orientation for dissociation of hydrogen on surfaces is when the molecular axis is parallel to the surface. Molecules whose axes are not parallel will be steered into the more favourable configuration, i.e., forced to rotate.

We think that more information than that reported here could be obtained by an analysis of diffraction probabilities, but many effects are masked by the attenuation of diffraction intensities when surface temperature and incident energy are increased [89, 90]. Future experiments should try to carefully measure this attenuation, and establish the precise limits for which the Debye–Waller model is applicable. Only then would one be able to disentangle thermal attenuation from other physical effects.

References

[1] Hulpke E (ed) 1992 *Helium Atom Scattering From Surfaces (Springer Series in Surface Sciences vol 27)* (Berlin: Springer)
[2] Farías D and Rieder K H 1998 *Rep. Prog. Phys.* **61** 1575
[3] Liebsch A and Harris J 1983 *Surf. Sci.* **130** L349
[4] Mattera L, Musenich R, Salvo C and Terreni S 1985 *Faraday Discuss. Chem. Soc.* **80** 115
[5] Kolodney E and Amirav A 1985 *Surf. Sci.* **155** 715
[6] Garibaldi U, Levi A C, Spadacini R and Tommei G E 1976 *Surf. Sci.* **55** 40
[7] Gerber R B, Yinnon A T, Shimoni Y and Kouri D J 1980 *J. Chem. Phys.* **73** 4397
[8] Rowe R G and Ehrlich G 1975 *J. Chem. Phys.* **63** 4643

[9] Boato G, Cantini P and Mattera L 1976 *J. Chem. Phys.* **65** 544
[10] Brusdeylins G and Toennies J P 1983 *Surf. Sci.* **126** 647
[11] Cowin J P, Yu C F, Sibener S J and Wharton L 1983 *J. Chem. Phys.* **79** 3537
[12] Berndt R, Toennies J P and Wöll C 1990 *J. Chem. Phys.* **92** 1468
[13] Goncharova L V, Braun J, Ermakov A V, Bishop G G, Smilgies D-M and Hinch B J 2001 *J. Chem. Phys.* **115** 7713
[14] Lapujoulade J and Perreau J 1983 *Phys. Scr.* T **4** 138
[15] Bertino M F, Graham A P, Rusin L Y and Toennies J P 1998 *J. Chem. Phys.* **109** 8036
[16] Benedek G, Bertino M F, Miret-Artes S and Toennies J P 1997 *Surf. Sci.* **377–9** 714
[17] Bertino M F, Miret-Artes S, Toennies J P and Benedek G 1997 *Phys. Rev.* B **56** 9964
[18] Wilzen L, Althoff F, Andersson S and Persson M 1991 *Phys. Rev.* B **43** 7003
[19] Gorse D, Salanon B, Fabre F, Kara A, Perreau J, Armand G and Lapujoulade J 1984 *Surf. Sci.* **147** 611
[20] Boato G, Cantini P and Tatarek R 1976 *J. Phys. F: Met. Phys.* **6** L237
[21] Luntz A, Mattera L, Rocca M, Tommasini F and Valbusa 1982 *Surf. Sci.* **120** L447
[22] Luntz A, Mattera L, Rocca M, Terreni S, Tommasini F and Valbusa 1983 *Surf. Sci.* **126** 695
[23] Hayward D O and Taylor A O 1986 *J. Phys. C: Solid State Phys.* **19** L309
[24] Bertino M F, Hofmann F and Toennies J P 1997 *J. Chem. Phys.* **106** 4327
[25] Engel T and Rieder K H 1981 *Surf. Sci.* **109** 140
[26] Cvetko D, Morgante A, Santaniello A and Tommasini F 1996 *J. Chem. Phys.* **104** 7778
[27] Parschau G, Kirsten E, Bischof A and Rieder K H 1989 *Phys. Rev.* B **40** 6012
[28] Farías D, Patting M and Rieder K H 2002 *J. Chem. Phys.* at press
[29] Farías D, Miranda R and Rieder K H 2002 *J. Chem. Phys.* submitted
[30] Lapujoulade J, Le Cruer Y, Lefort M, Lejay Y and Mauriel E 1981 *Surf. Sci.* **103** L85
[31] Yu C, Whaley K B, Hogg C S and Sibener S J 1985 *J. Chem. Phys.* **83** 4217
Whaley K B, Yu C, Hogg C S, Light J C and Sibener S J 1985 *J. Chem. Phys.* **83** 4235
[32] Gerber R B, Beard L H and Kouri D J 1981 *J. Chem. Phys.* **74** 4709
[33] Fitz D E, Beard L H and Kouri D J 1981 *Chem. Phys.* **59** 257
[34] Kouri D J and Gerber R B 1982 *Israel J. Chem.* **22** 321
[35] Schinke R 1982 *J. Chem. Phys.* **76** 2352
Schinke R 1982 *Chem. Phys. Lett.* **87** 438
[36] Hubbard L M and Miller W H 1983 *J. Chem. Phys.* **78** 1801
[37] Whaley K B and Light J C 1984 *J. Chem. Phys.* **81** 3334
[38] Jackson B and Metiu H 1986 *J. Chem. Phys.* **84** 3535
[39] Drolshagen G, Kaufhold A and Toennies J P 1985 *J. Chem. Phys.* **83** 827
[40] Wolken G 1973 *J. Chem. Phys.* **59** 1159
Wolken G 1973 *Chem. Phys. Lett.* **21** 373
[41] Wolken G 1975 *J. Chem. Phys.* **62** 2730
[42] Cruz A J and Jackson B 1989 *J. Chem. Phys.* **91** 4985
[43] Rendulic D, Anger G and Winkler A 1989 *Surf. Sci.* **208** 404
[44] Rettner C T, Auerbach D J and Michelsen H A 1992 *Phys. Rev. Lett.* **68** 1164
Rettner C T, Auerbach D J and Michelsen H A 1992 *Phys. Rev. Lett.* **68** 2547
[45] Rettner C T 1992 *Phys. Rev. Lett.* **69** 383
[46] Darling G R and Holloway S 1995 *Rep. Prog. Phys.* **58** 1595
[47] Gross A 1998 *Surf. Sci. Rep.* **32** 291
[48] Kroes G J 1999 *Prog. Surf. Sci.* **60** 1
[49] Diño W A, Kasai H and Okiji A 2000 *Prog. Surf. Sci.* **63** 63
[50] Busnengo H F, Dong W and Salin A 2000 *Chem. Phys. Lett.* **320** 328
Busnengo H F, Salin A and Dong W 2000 *J. Chem. Phys.* **112** 7641
Busnengo H F, Crespos C, Dong W, Salin A and Rayez J C 2001 *Phys. Rev.* B **63** 041402(R)
[51] Hofmann F, Manson J R and Toennies J P 1994 *J. Chem. Phys.* **101** 10 155
[52] Toennies J P 1991 *Surface Phonons* ed W Kress and F W de Wette (Berlin: Springer) pp 111–66
[53] Miller D R 1988 *Atomic and Molecular Beam Methods* vol 1, ed G Scoles (Oxford: Oxford University Press) pp 14–53
[54] Bertino M F and Toennies J P 1999 *J. Chem. Phys.* **110** 9186
[55] Christmann K 1988 *Surf. Sci. Rep.* **9**
[56] Engel T and Rieder K H 1981 *Surf. Sci.* **109** 140
[57] Hanbicki A T, Baddorf A P, Plummer E W, Hammer B and Scheffler M 1995 *Surf. Sci.* **331–3** 811
Hanbicki A, Davis H L, Baddorf A P, Poker D B and Plummer E W 1996 *Surf. Sci.* **365** L639

[58] Lui S C, Davenport J W, Plummer E W, Zehner D M and Ferrando G W 1990 *Phys. Rev.* B **42** 1582
[59] Beutl M, Rendulic K and Castro G R 1995 *J. Chem. Soc. Faraday Trans.* **91** 3639
[60] Davis H L and Noonan J R 1985 *Phys. Rev. Lett.* **54** 566
Yalisove S M and Graham W R 1987 *Surf. Sci.* **183** 556
Mullins D R and Overbury S H 1988 *Surf. Sci.* **199** 141
[61] Pollard J E, Trevor D J, Lee Y T and Shirley D A 1982 *J. Chem. Phys.* **77** 4819
[62] Kern K, David R and Comsa G 1985 *J. Chem. Phys.* **82** 5673
[63] Winkelmann K 1979 *11th Int. Symp. on Rarefied Gas Dynamics* (Commissariat a L'energie Atomique: Paris)
[64] Faubel M, Gianturco F A, Ragnetti F, Rusin L Y, Sondermann F and Tappe U 1994 *J. Chem. Phys.* **101** 8800
[65] Huber K P and Herzberg G 1978 *Molecular Spectra and Molecular Structure* vol 4 (New York: Van Nostrand)
[66] Rettner C T, Auerbach D J and Michelsen H A 1992 *Phys. Rev. Lett.* **68** 1164
[67] Hayden B E and Lamont C L A 1991 *Surf. Sci.* **243** 31
[68] Pauly H 2000 *Atom, Molecule, and Cluster Beams I (Springer Series in Atomic, Optical, and Plasma Physics vol 2)* (Berlin: Springer)
[69] Massey H S W, Burhop E H S and Gilbody H B 1969 *Electronic and Ionic Impact Phenomena* 2nd edn, vol 1 (Oxford: Clarendon) pp 128–30
Massey H S W, Burhop E H S and Gilbody H B 1969 *Electronic and Ionic Impact Phenomena* 2nd edn, vol 2 (Oxford: Clarendon) pp 909–18
[70] Manson J R 1992 *Helium Atom Scattering from Surfaces* ed E Hulpke (Berlin: Springer) pp 195–200
[71] Gumhalter B 2001 *Phys. Rep.* **351** 1
[72] Beeby J L 1971 *J. Phys. C: Solid State Phys.* **4** L359
[73] Andersson S and Kus B 1970 *Solid State Commun.* **8** 1885
[74] Liebsch A and Harris J 1981 *Surf. Sci.* **111** L721
[75] Halstead D and Holloway S 1988 *J. Chem. Phys.* **88** 7197
[76] Gross A and Scheffler M 1996 *Chem. Phys. Lett.* **263** 567
[77] Watts E and Sitz G O 1999 *J. Phys.: Condens. Matter* **111** 9791
[78] Watts E and Sitz G O 2001 *J. Chem. Phys.* **114** 4171
[79] Murphy M J and Hodgson A 1998 *J. Chem. Phys.* **108** 4199
[80] Garibaldi U, Levi A C, Spadacini R and Tommei G E 1975 *Surf. Sci.* **48** 649
[81] Rieder K H 1992 *Helium Atom Scattering from Surfaces* ed E Hulpke (Berlin: Springer) pp 41–69
[82] García N, Barker J A and Rieder K H 1983 *Solid State Commun.* **45** 567
[83] Diño W A, Fukutani K, Okano T, Kasai H, Okiji A, Farías D and Rieder K H 2001 *J. Phys. Soc. Japan* **70** 3491
[84] Lapujoulade J and Perreau J 1982 *Surf. Sci.* **122** 341
[85] Evett A E and Margenau H 1953 *Phys. Rev.* B **90** 1021
[86] Mason E A and Hirschfelder J O 1957 *J. Chem. Phys.* **26** 757
[87] McDaniel E W 1989 *Atomic Collisions: Electronic and Photon Projectiles* (New York: Wiley) section 8-2
[88] Diño W A, Kasai H and Okiji A 1995 *J. Phys. Soc. Japan* **64** 2478
[89] Busnengo H F, Dong W, Sautet P and Salin A 2001 *Phys. Rev. Lett.* **87** 127601
[90] Wang Z S, Darling G R and Holloway S 2001 *Phys. Rev. Lett.* **87** 226102